Check for updates

In situ coupling of Ti$_2$O with rutile TiO$_2$ as a core–shell structure and its photocatalysis performance†

Qingjie Wang,[ab] Jiajie Fan, [ID] [ab] Shilin Zhang, [ID] [ab] Yifan Yun,[ab] Jinhua Zhang,[ab] Peng Zhang, [ID] [abc] Junhua Hu, [ID] *[ab] Lijie Wang‡*[abc] and Guosheng Shao*[abd]

The fabrication of high-performance, low-cost photocatalysis materials, which absorb in the visible-light region, is of significance for their practical applications. A Ti$_2$O@TiO$_2$ (rutile) core–shell structure was fabricated through dehydrogenation and oxidation from TiH$_2$. Thermal analysis indicates that a bimodal oxidation behavior accounts for the formation of a bi-phasic composite. The response of the composite under UV and visible light was measured by PL (photoluminescence) spectra and a photo-degradation test. A pronounced improvement in photo-degradation performance is attributed to the synergistic function of exciton separation of the core–shell structure and the visible light response of the Ti$_2$O cores.

1. Introduction

A visible light response of photocatalysts induced by localized surface plasmon resonance (SPR) has been commonly observed in noble metal nanostructures since it was first reported for synthesized gold colloids by Faraday more than 150 years ago. The surface plasmon resonance phenomena observed in noble metal nanoclusters such as Au, Ag, Cu, Pt, and Pd provide a promising strategy for enhancing the photocatalytic efficiency of semiconductors by loading these nanoclusters on to the semiconductor surfaces.[1–3] The resonance between the metal nanostructures depends on the interaction of their free electrons with the oscillating electromagnetic field of light. Therefore, the electron concentration and effective mass of the carriers determines the performance of the plasmonic material systems. As the free electron concentration in metallic materials is always fixed, the SPR of the metal nanoparticles is always tuned by the size effect and geometric factors. For instance, gold (Au) nanostructures are the most systematically investigated due to their chemical inertness and relative synthetic accessibility. Spherical gold nanoparticles with diameters ranging from 3 to 50 nm exhibit SPR at visible-light wavelengths.[4]

[a]School of Materials Science and Engineering, Zhengzhou University, Zhengzhou 450002, China. E-mail: hujh@zzu.edu.cn; lijiewang@epfl.ch; Gsshao@zzu.edu.cn

[b]State Centre for International Cooperation on Designer Low-carbon and Environmental Materials, Zhengzhou University, Zhengzhou 450001, China

[c]Henan Province Industrial Technology Research Institute of Resources and Materials, Zhengzhou University, Zhengzhou 450002, China

[d]Institute for Renewable Energy and Environmental Technologies, University of Bolton, Bolton BL3 5AB, UK

† Electronic supplementary information (ESI) available. See DOI: 10.1039/c7ra10347f

‡ Ecole Polytech Fed Lausanne, Lausanne Ctr Ultrafast Sci LACUS, LSU, ISIC, FSB, Stn 6, CH-1015 Lausanne, Switzerland.

Hollow or anisotropic gold nanostructures can exhibit multiple SPR modes over visible to near infrared (NIR) wavelengths. Anisotropic structures (*e.g.*, nanorods) can support multiple SPR modes along different axes of the nanostructure.[5]

Many classes of materials such as doped semiconductors and metal chalcogenides exhibit plasmonic behavior in their corresponding optical band.[1,2] Although these plasmonic materials share identical physical basis with elemental metals, their stoichiometry endows them with more freedom to tune the electronic structure by doping and other band engineering approaches. However, none of the plasmonic materials exhibit optical properties superior to those of silver and gold. The discovery and study of alternative materials, other than plasmonic gold and silver, that interact with visible light is still a rapidly growing field of research. For materials to be integrated in realistic applications of photocatalysis, they should meet the following requirements: (i) low cost, (ii) ease of fabrication, and (iii) tunable optical absorption in visible region. Herein, oxygen-deficient titanium oxide Ti$_2$O is proposed as a novel photocatalyst material for visible light absorption. The employed precursor was commercially available TiH$_2$ powder. A bimodal oxidation behavior resulted in the formation of the TiO$_2$@Ti$_2$O core–shell composite. An evident enhancement in the visible light absorption due to the formation of Ti$_2$O was observed. A photodegradation study was also employed to exhibit the performance of the Ti$_2$O co-catalyst. The simple and feasible fabrication method demonstrates the possibility of practical applications of these photocatalysts in the future.

2. Experiment

In a typical preparation process, 2 g TiH$_2$ (Sigma-Aldrich, 99%) was first milled by a planetary ball milling mixer for 2 h (400 rpm), containing 30 g agate balls. Subsequently, the milled TiH$_2$

was treated at 550–640 °C for 2 h, 6 h and 10 h in a tube furnace. The heating rate was set to 2 °C min^{-1}. Then, the pre-treated TiH$_2$ powder was placed in a sealed container and the heat treatment was carried out without any protective gas. It should be noted that TiH$_2$ is an industrial raw material for the production of H$_2$ in metallurgy as it provides an oxygen-limited atmosphere.

The morphologies and structures of the as-prepared samples were analyzed using a field emission scanning electron microscope (FESEM; JSM-7500F) and a high resolution transmission electron microscope (TEM; FEI Tecnai G2 F20) with an accelerating voltage of 200 kV. Typical powder XRD patterns of the as-prepared samples were obtained using a D/max 2500 XRD diffractometer (Rigaku Ultima IV) with Cu Kα radiation (λ = 0.1541 nm) from 20° to 80° at a scanning rate of 4° min^{-1}. The content of the different phases was evaluated by XRD patterns. The relative content was obtained by comparing the intensity of the dominant diffraction peaks. The analysis software was integrated into the XRD (Rigaku Ultima IV) equipment. The UV-vis absorption of the as-prepared samples in the range from 200 to 800 nm was measured using a Shimadzu, model UV3600, spectrophotometer equipped with an integrating sphere, in which standard BaSO$_4$ powder was used as a reference. X-ray photoelectron spectroscopy (XPS) was performed on an ESCA-LAB 250 spectrometer (Thermo Scientific Ltd. England) with Al Kα (hv = 1486.6 eV) radiation as the source. Photoluminescence spectra were recorded to characterize the electron–hole recombination probabilities with a Jobin Yvon HR800 micro-Raman spectrometer using a He–Cd 325 nm laser.

The photocatalytic activity under visible irradiation of the as-prepared TiO$_2$/Ti$_2$O composites was evaluated by performing the degradation of a methylene blue (MB) aqueous solution under visible light irradiation (>420 nm). Briefly, 50 mg as-synthesized samples were mixed with 80 mL 100 mg L^{-1} MB aqueous solution in a transparent quartz container with a volume of 100 mL. Prior to illumination, the suspension was ultra-sonicated for 1 min to ensure that the photocatalyst was highly dispersed, followed by stirring for 30 min in the dark at room temperature to establish an adsorption–desorption equilibrium between MB and the surface of the photocatalyst. Following this, the container was placed under a 300 W xenon lamp (Beijing Perfectlight Co. Ltd, the UV-vis spectrum was shown in Fig. S1†) equipped with an ultraviolet cutoff filter (λ > 420 nm), which was used as the visible light source. During illumination, photocatalytic degradation of the MB aqueous solution was measured by an UV-Vis spectrophotometer (UV3600 spectrophotometer, Shimadzu) at given intervals (30 min). As a comparison, the photocatalytic degradation of the MB aqueous solution over pure rutile TiO$_2$ was also conducted under identical conditions. The percent degradation percentage of the MB solution was calculated in the same way as described in ref. 6.

3. Results

Following thermal treatment, the phase composition of the resultant powder was tested by XRD and the results are shown in Fig. 1. Based on the results, the formation of Ti$_2$O was confirmed. As the heating temperature was increased, the residual TiH$_2$ phase disappeared and the rutile-phase TiO$_2$ gradually increased. When the temperature was increased to 610 °C, the resultant powder demonstrated a dual-phase structure. At the temperature of 580 °C, prolonged treatment time also resulted in the formation of Ti$_2$O and TiO$_2$ composites. The structure of Ti$_2$O can be described in terms of a hexagonal close-packed arrangement of titanium atoms (c/a = 1.637), in which the oxygen atoms are ordered so as to occupy every second layer of octahedral interstices normal to the c-axis. The unit cell is shown in Fig. 1b.[7] It is well-known that anatase TiO$_2$ is a very effective photocatalyst. According to anatase ICDD (21-1272), the first and second XRD peaks of anatase are located at 2-theta values of 25.28° and 48.04°, respectively. However, in the XRD spectra of the as-prepared composite, there is no peak observed corresponding to these 2-theta values. Thus, we can exclude the formation of this phase. The as-prepared photocatalyst displays a high stability exposed in air for months. Following refinement of the XRD patterns, the phase composition ratios were calculated and are displayed in Fig. 1c.

Fig. 2 shows the morphology of the as-synthesized TiO$_2$/Ti$_2$O composite. The raw TiH$_2$ is irregular in shape with sizes measuring of several tens of micrometers. After milling and heat treatment, the powder particles showed nearly-spherical morphologies with rough surfaces (Fig. 2b). The internal HRTEM image of the selected area was further characterized (Fig. 2c). The outer layer was a rutile TiO$_2$ shell, as indicated in regions A, B, and D. For region A, d = 3.24 nm is attributed to rutile (R) (110), with an angle of 67.5° to R (101), whose lattice fringe was 2.50 nm. The internal phase shows a typical lattice spacing, corresponding to Ti$_2$O. These results confirm that a TiO$_2$ shell@Ti$_2$O core structure was formed.

To understand the formation process of the core–shell structure, a differential scanning calorimetry (DSC) analyses was carried out. In Fig. 3, the bimodal oxidation behavior is represented by a dotted curve. The exothermic reaction starting at 510 °C corresponds to the dehydrogenation of TiH$_2$. The subsequent reaction was the further oxidation of Ti$_2$O to rutile phase. Both reactions occurred continuously and resulted in the dual phase composite.[8] The reaction route is illustrated in the left inset in Fig. 3.

The photoresponse of the as-synthesized samples, which were heated for 6 h at different temperatures, was measured using a UV-vis spectrophotometer. The samples obtained at 640–550 °C for 6 h exhibited a typical UV-vis reflectance spectrum with a primary cut-off edge at ∼410 nm, corresponding to the intrinsic band gap of 3.0 eV for rutile.[9] As observed, the SPR-like visible-light absorption band at ∼400–500 nm was present in the spectrum. The position and intensity of the absorption peaks in the visible light region depend on the heat-treatment temperature, which originates from the grain-size effect and is consistent with other SPR systems.[10,11] The rutile TiO$_2$ is transparent, *i.e.*, it does not absorb visible light. As a consequence, the improved utilization of photo energy was due to the existence of Ti$_2$O phase in a composite. The sample synthesized at 550 °C for 6 h showed
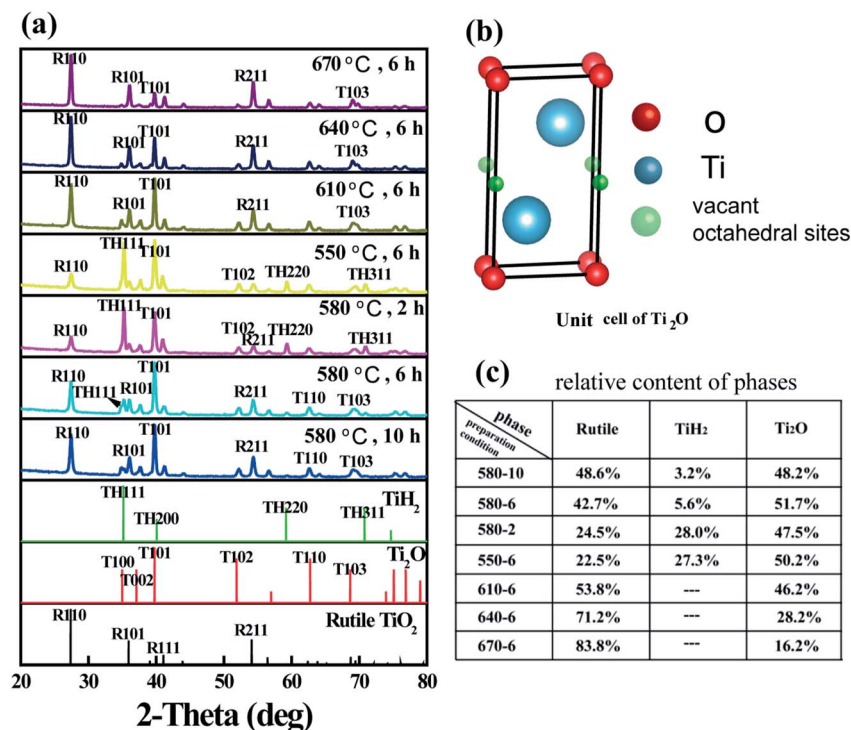
Fig. 1 (a) XRD patterns of the samples heated at different condition (indicated on the corresponding patterns). T: Ti_2O (ICDD 01-073-1581), TH: TiH_2 (ICDD 03-065-0934), R: rutile TiO_2 (ICDD 01-086-0147). (b) The unit cell of Ti_2O phase. (c) The relative contents of different phases.

extra broad visible-light absorption at 500–800 nm, owing to the residual TiH_2 phase.[12] The inset in Fig. 4a shows that samples fabricated at 580 °C for 2–10 h demonstrated identical phenomena (details in Fig. S2a†).

It has been shown that heterojunctions are usually favorable for the separation of photo-induced holes and electrons. To address the effect of the $TiO_2@Ti_2O$ core–shell structure on the separation of the electrons and holes, the PL spectra of core–shell structure films excited at 325 nm are shown in Fig. 4b. A broad PL band in 400–700 nm represents the radiative recombination of self-trapped excitons.[13] The peaks at 425 nm and 540 nm were ascribed to a strongly localized state (based on oxygen vacancies) and the recombination of free electrons with the trapped holes in the rutile phase, respectively.[14,15] With prolonged treatment time, a pronounced intensity decrease was observed in the spectrum. The loss in intensity demonstrates the enhancement in exciton separation. The transformation
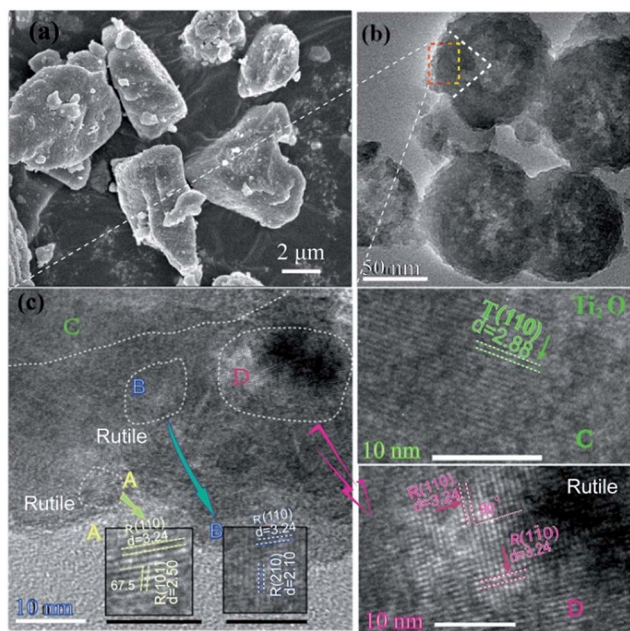

Fig. 2 (a) Morphology of milled TiH_2. (b) Morphology of the synthesized composite. (c) HRTEM of selected area. The detail on the lattice fringe in the selected area was shown in A–D.
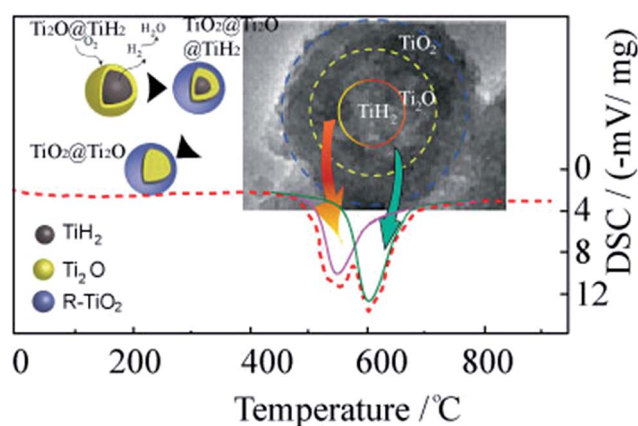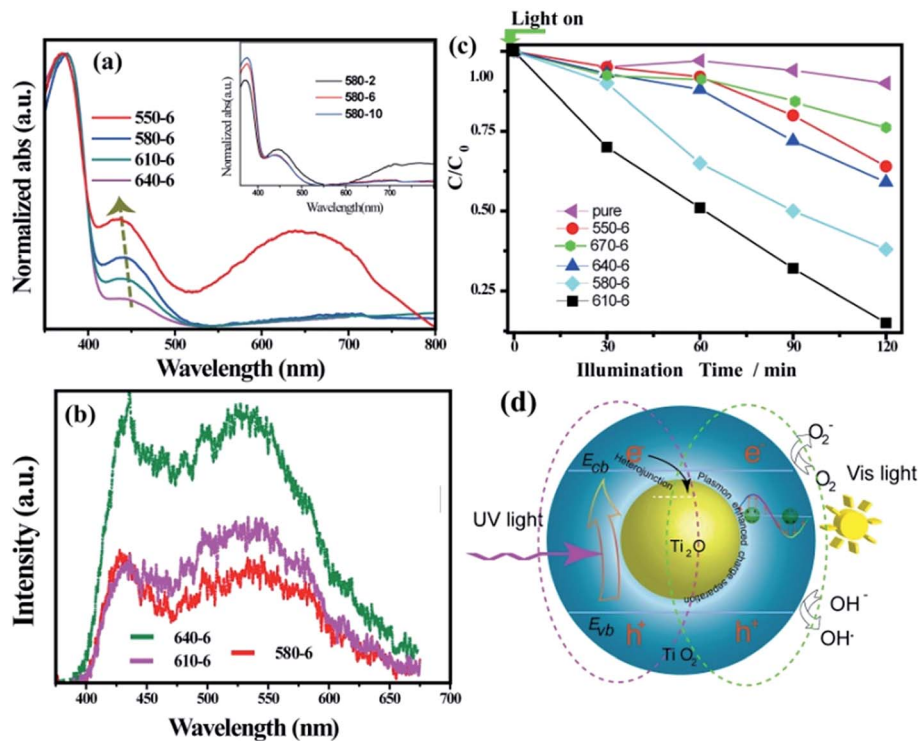

Fig. 3 DSC curves of TiH_2.

Fig. 4 (a) UV-vis absorption spectra of the as-synthesized samples. The inset in (a) is also shown separately in Fig. S2a† (b) PL spectra of the as-synthesized samples. The relative content of Ti_2O in composite is shown in Fig. S2b.† (c) Comparison of photocatalytic degradation of aqueous solution of MB under visible light irradiation. Fig. S3† shows the time-dependent absorption spectral pattern of MB samples obtained for the sample over 6 h@610 °C. $T = 0$ is when the light is turned on. The spectra for commercial rutile TiO_2 (pure) is shown as a comparison. (d) The postulated mechanism for the UV light and visible light response of composite.

from Ti_2O to rutile TiO_2 would shrink the contact interface of the two phases. As a result, the sample 640-6 shows an intense luminance peak. Generally, a diffusive PL spectrum is a characteristic for rutile TiO_2.[13,15] However, a pronounced dip in the PL spectra is observed (Fig. 4b), which is located within the band of the SPR-like absorption. A more probable explanation could be the strongly enhanced field effect near the core–shell interface,[16] where the electron–hole separation of photoexcited TiO_2 can be promoted through plasmon exciton coupling.[17–19]

The photo catalytic activity of the as-synthesized $Ti_2O@TiO_2$ composite samples was evaluated by the degradation of methylene blue (MB) under visible light (>420 nm) irradiation. The degradation curves are displayed in Fig. 4c. It could be observed that after visible light irradiation for 2 h, the degradation efficiencies of the MB aqueous solution were about 38%, 40%, 61% and 90% for the samples 6 h@550 °C, 6 h@640 °C, 6 h@580 °C and 6 h@610 °C, respectively. In comparison, pure rutile TiO_2 (Sinopharm Group, 100 nm) showed poor degradation activity of less than 10% over 2 h due to its negligible harvesting ability of visible light. Clearly, the synthesized $Ti_2O@TiO_2$ composite exhibited a much better photocatalytic performance; the sample obtained at 610 °C for 6 h displayed the best photocatalytic activity among all the samples (Fig. S3†). Thus, an appropriate Ti_2O/TiO_2 ratio is evidently required for the degradation of MB. This great enhancement is attributed to the

synergy of exciton separation of core–shell structure and visible light harvesting of Ti_2O cores.

A mechanism of the UV light and visible light response of composite is postulated in Fig. 4d. The band diagram calculation shows that Ti_2O is metallic (Fig. 5). It should be noted that the relative location of the conductive band (CB) is also defined by the DFT method. Under UV light, rutile TiO_2 undergoes excitation. Due to the relatively low CB location of Ti_2O, a Schottky junction is established on the core–shell interface and the excited electrons would be collected by the Ti_2O core. Thus, the promoted separation of the electron–hole pairs and the resulting relatively low PL intensity were obtained (Fig. 4b). Irradiated by visible light, the rutile TiO_2 is transparent to light with wavelengths >420 nm, with only the TiO_2 core being
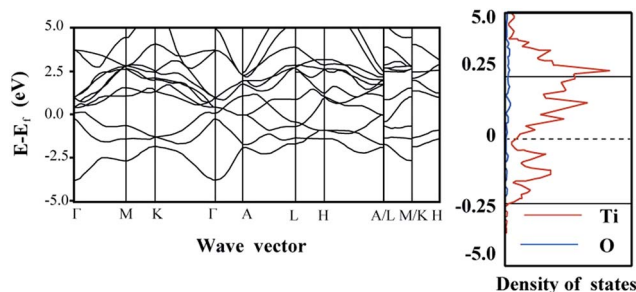

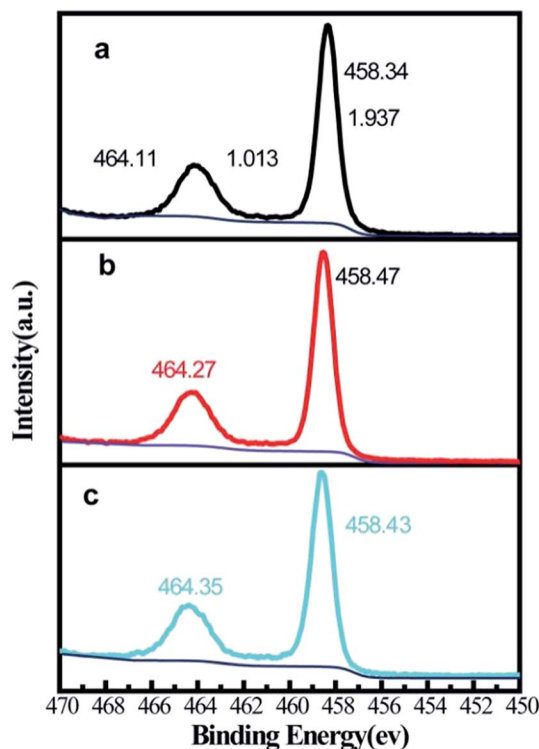**Fig. 5** Band diagram and density of state (DOS) of Ti_2O.

Fig. 6 XPS spectra of Ti 2p. (a) 550-6; (b) 610-6; (c) 640-6.

excited. However, the excited electrons would stay in the core. The holes captured by the rutile phase react with the MB molecules. Due to the limited diffusion length of the holes, the

Fig. 7 XPS spectra of O 1s. (a) 550-6; (b) 610-6; (c) 640-6.

excessively oxidized sample (640-6) with thicker rutile phase show a low degradation ratio. The 610-6 sample demonstrated the most optimized property (Fig. 4c).

It is possible that the visible light absorption can be induced by the defect states of rutile phase. Surface chemical state analysis was performed using XPS. As shown in Fig. 6, after eliminating the background noise, Ti 2p peaks show high symmetry and a narrow full width at half maximum (<2 eV), which demonstrates the full oxidation state of Ti. The positions of Ti $2p_{3/2}$ and Ti $2p_{1/2}$ are almost identical. It should be noted that the acceptable error margin for XPS should be within 0.2 eV.[20] As shown in Fig. 6, the different treatments did not generate a reduced state of Ti. This proved that a stable fabrication environment was established. The chemical state of O was measured for some samples by XPS (Fig. 7). As shown in Fig. 7a, the O 1s spectrum is deconvoluted into three peaks at 531.42, 530.26 and 529.73 eV. The peaks at 531.42 and 529.73 eV is ascribed to surficial –OH and Ti (+4)–O lattice bonding, respectively. The peak at 530.26 eV was the native defect for oxides.[21] The influence of treatment temperature on the native oxygen defect was negligible concerning the position (within 0.2 eV) and intensity. However, it is observed that both the degradation performance and the visible light absorbance changed with the treatment temperature. Logically, we are unable ascribe the enhancement in visible light absorption and MB degradation to the formation of defect states.

4. Conclusions

A unique $Ti_2O@TiO_2$ composite was fabricated through the dehydrogenation–oxidation reaction of TiH_2. The content of the Ti_2O produced depends on the thermal treatment condition. A pronounced enhancement in the absorption spectra centered at 420 nm demonstrates a SPR-like response of the composite. The formation of a heterostructure and a broad range of visible light harvesting promote the carrier separation. Under visible light irradiation for 2 h, the degradation ratio of the MB aqueous solution was about 90% for the optimized composites. By comparison, pure rutile showed poor degradation activity of less than 10% over 2 h, which corresponds to its negligible harvesting ability of visible light. Although further investigation should be carried out on the novel Ti_2O photocatalysis materials, this study demonstrates a simple and economical method to develop a highly active photocatalyst under visible light irradiation.

Conflicts of interest

There are no conflicts to declare.

Acknowledgements

References

1 X. Liu and M. T. Swihart, Heavily-doped colloidal semiconductor and metal oxide nanocrystals: an emerging new class of plasmonic nanomaterials, *Chem. Soc. Rev.*, 2014, **43**, 3908–3920.

2 G. V. Naik, V. M. Shalaev and A. Boltasseva, Alternative Plasmonic Materials: Beyond Gold and Silver, *Adv. Mater.*, 2013, **25**, 3264–3294.

3 Y. Wang, J. G. Yu, W. Xiao and Q. Li, Microwave-assisted hydrothermal synthesis of graphene based $Au-TiO_2$ photocatalysts for efficient visible-light hydrogen production, *J. Mater. Chem. A*, 2014, **2**, 3847–3855.

4 E. Ozbay, Plasmonics: merging photonics and electronics at nanoscale dimensions, *Science*, 2006, **311**, 189–193.

5 H. J. Chen, L. Shao, Q. Li and J. F. Wang, Gold nanorods and their plasmonic properties, *Chem. Soc. Rev.*, 2013, **42**, 2679–2724.

6 L. Wang, J. Fan, Z. Cao, Y. Zheng, Z. Yao, G. Shao and J. Hu, Fabrication of predominantly Mn^{4+} doped TiO_2 nanoparticles under equilibrium conditions and their application as visible-light photocatalyts, *Chem.–Asian J.*, 2014, **9**, 1904–1912.

7 A. Jostsons and P. G. Mcdouga, Fault Structures in Ti_2O, *Phys. Status Solidi*, 1968, **29**, 873–889.

8 Y. Wang, N. Zhang, X. Ren, H. Hou and B. Wang, Behavior and rule of titanium hydride dynamic decomposition, *Materials Science and Engineering of Powder Metallurgy*, 2011, **16**, 795–798.

9 G. J. Kalaivani and S. K. Suja, TiO_2 (rutile) embedded inulin—a versatile bio-nanocomposite for photocatalytic degradation of methylene blue, *Carbohydr. Polym.*, 2016, **143**, 51–60.

10 I. Kriegel, C. Jiang, J. Rodríguez-Fernandez, R. D. Schaller, D. V. Talapin, E. Como and J. Feldmann, Tuning the Excitonic and Plasmonic Properties of Copper Chalcogenide Nanocrystals, *J. Am. Chem. Soc.*, 2012, **134**, 1583–1590.

11 W. Han, L. Yi, N. Zhao, A. Tang, M. Gao and Z. Tang, Synthesis and Shape-tailoring of the Copper Sulfide/Indium Sulfide-Based Nanocrystals, *J. Am. Chem. Soc.*, 2008, **130**, 13152–13161.

12 L. R. Grabstanowicz, S. Gao, T. Li, R. M. Rickard, T. Rajh, Di-J. Liu and T. Xu, Facile Oxidative Conversion of TiH_2 to High-Concentration Ti^{3+}-Self Doped Rutile TiO_2 with Visible-Light Photoactivity, *Inorg. Chem.*, 2013, **52**, 3884–3890.

13 C. Wang, X. Zhang, C. Shao, Y. Zhang, J. Yang, P. Sun, X. Liu, H. Liu, Y. Liu, T. Xie and D. Wang, Rutile TiO_2 nano wires on anatase TiO_2 nano fibers: a branched heterostructured photocatalysts via interface assistance fabrication approach, *J. Colloid Interface Sci.*, 2011, **363**, 157–164.

14 Y. Yamada and Y. Kanemitsu, Determination of electron and hole lifetimes of rutile and anatase TiO_2 single crystals, *Appl. Phys. Lett.*, 2012, **101**, 1339071–1339074.

15 M. Nasr, A. A. Chaaya, N. Abboud, M. Bechelany, R. Viter, C. Eid, A. Khoury and P. Miele, Photoluminescence: a very sensitive tool to detect the presence of anatase in rutile phase electrospun TiO_2 nanofibers, *Superlattices Microstruct.*, 2015, **77**, 18–24.

16 Z. Zhang, Z. Wang, S.-W. Cao and C. Xue, Au/Pt Nanoparticle-Decorated TiO_2 Nanofibers with Plasmon Enhanced Photocatalytic Activities for Solar-to-Fuel Conversion, *J. Phys. Chem. C*, 2013, **117**, 25939–25947.

17 J. Hu, P. Wang, P. Liu, G. Cao, Q. Wang, M. Wei, *et al.*, In Situ Fabrication of Nano Porous NiO-Capped Ni3P film as Anode for Li-Ion Battery with Different Lithiation Path and Significantly Enhanced Electrochemical Performance, *Electrochim. Acta*, 2016, **220**, 258–266.

18 Z. W. Seh, S. Liu, M. Low, S. Zhang, Z. Liu, A. Mlayah and M. Han, Janus $Au-TiO_2$ Photocatalysts with Strong Localization of Plasmonic Near-Fields for Efficient Visible-Light Hydrogen Generation, *Adv. Mater.*, 2012, **24**, 2310–2314.

19 S. W. Cao, Z. Yin, J. Barber, F. Boey, S. C. J. Loo and C. Xue, Preparation of $Au-BiVO_4$ Heterogeneous Nanostructures as Highly Efficient Visible-Light Photo catalysts, *ACS Appl. Mater. Interfaces*, 2012, **4**, 418–423.

20 J. Hu, L. Yang, G. Cao, Y. Yun, *et al.*, On the oxidation behavior of (Zr,Nb)(2)Fe under simulated nuclear reactor conditions, *Corros. Sci.*, 2016, **112**, 718–723.

21 J. Hu, L. Wang, P. Zhang, C. Liang and G. Shao, Construction of solid-state Z-scheme carbon-modified TiO_2/WO_3 nanofibers with enhanced photocatalytic hydrogen production, *J. Power Sources*, 2016, **328**, 28–36.